Supporting Information for "Identifying the Origins of Nanoplastics in the Abyssal South Atlantic Using Backtracking Lagrangian Simulations with Fragmentation"

Claudio Pierard[1], Florian Meirer[2], Erik van Sebille[1]

[1]Utrecht University, Institute for Marine and Atmospheric Research, Princetonplein 5, 3584 CC Utrecht, Netherlands

[2]Utrecht University, Debye Institute for Nanomaterials Science & Institute for Sustainable and Circular Chemistry, Inorganic Chemistry and Catalysis, Universiteitsweg 99, 3584 CG Utrecht, Netherlands

Contents of this file

1. Text S1 to S2
2. Figures S1 to S2
3. Table S1

Text S1. Scaling analysis of nano- and microplastics Several forces act on microplastics and nanoplastics, and some of them dominate over others. To understand this dynamic, we performed a scaling analysis to establish what forces are dominant at different length scales of the particles. Following a similar approach as Russel, Saville, and Schowalter (1989), we analyzed the magnitudes of characteristic forces acting on spherical particles in a colloidal system. For plastic particles, the dominant forces responsible for the transport are the Brownian force and the viscous and inertial forces (Al Harraq &

Bharti, 2022). We ignored the inter-particle attracting and repelling forces because the volume concentration of plastic in the ocean is low (Sutherland et al., 2023). From the forces acting on plastic particles, the Brownian force magnitude is $\mathcal{O}(k_B T/R)$, where k_B is the Boltzmann constant ($1.381 \times 10^{-23}\,\mathrm{J\,K^{-1}}$), T is the absolute temperature, and R is the characteristic radius of the particles. The viscous force due to Stokes has a magnitude $\mathcal{O}(\mu U R)$, where μ is the dynamic viscosity of water and U is the characteristic velocity of the particles moving through the fluid. The inertial force magnitude is $\mathcal{O}(\rho U^2 R^2)$, where ρ is the density of the particle. The buoyancy force, due to the difference between the density of the particle and the fluid $\Delta\rho$, and gravitational acceleration g, is $\mathcal{O}(g \Delta\rho R^3)$.

In Table S1 we compare the magnitudes of the forces acting on a particle of a characteristic radius. We compared particles with radius $R = [0.01, 0.1, 1, 10, 100]$ µm. Table S1 shows that for particles of radius 0.01 µm to 0.1 µm the Brownian force and viscous force dominate over the buoyancy and inertial forces. For particles with 1 µm in radius, the Brownian, viscous, and buoyant forces are of equal order of magnitude, but particles remain non-inertial. For particles with $R = 10$ µm to 100 µm, the buoyant and viscous forces dominate over the Brownian and inertial forces, i.e. the sinking controls the dynamics of these particles. The scaling analysis suggests that particles with $R \leq 1$ µm can be considered to be in a colloidal system, where viscous and Brownian forces control the dynamics of the particles. Particles with $R > 1$ µm depart from this colloidal state by the increasing dominance of the buoyant force in their transport.

Text S2. Comparison between simulations with maximum size class $k = 2$, $k = 3$ and $k = 4$. We compared simulations with three maximum-size classes in the fragmentation scheme. We fixed the fragmenting timescale $\lambda_f = 1000$ days and performed three independent simulations setting the limit to the maximum number of size classes the particles can fragment into, k_{max}. The first simulation had a $k_{max} = 2$, therefore it follows particles that fragment down to $1/8^2$ of the pre-fragmentation mass M. The second simulation had a $k_{max} = 3$, which is the one used in the main study. The simulation with $k_{max} = 3$ considers the particles that fragment down $1/8^3$ of M. The third simulation had a $k_{max} = 4$, which considers particles with down to $1/8^4$ of M.

In Figure S2 we compare the simulations with different k_{max}. In Figure S2A, we show the empirical density distribution function for the particle radius of particles coming from the surface. In general, the three simulations have similar shape distributions, but $k_{max} = 4$ has more particles with $R > 1 \times 10^{-4}\,\mathrm{m}$, and fewer particles for R between $1 \times 10^{-6}\,\mathrm{m}$ and $1 \times 10^{-4}\,\mathrm{m}$, compared to $k_{max} = 3$ and $k_{max} = 2$. For example, $k_{max} = 2$ has 0.2% of particles with $R < 1 \times 10^{-6}\,\mathrm{m}$, 98% with R between $1 \times 10^{-6}\,\mathrm{m}$ and $1 \times 10^{-4}\,\mathrm{m}$; and 1.8% with radius $R > 1 \times 10^{-4}\,\mathrm{m}$. In comparison, $k_{max} = 4$ has zero particles with $R < 1 \times 10^{-6}\,\mathrm{m}$, 76% with R between $1 \times 10^{-6}\,\mathrm{m}$ and $1 \times 10^{-4}\,\mathrm{m}$; and 24% with radius $R > 1 \times 10^{-4}\,\mathrm{m}$.

Figure S2B compares the time it takes for the particles to reach the sampling location at 5,100 m deep from the surface. The ECDF plot shows that for big k_{max}, the total drift time of particles is reduced compared to the simulations with smaller k_{max}. This implies that increasing the number of size classes in the simulation decreases the time the particles need to reach the surface size distribution. This is equivalent to decreasing the fragmenting timescale λ_f in the simulations (see Figure 6).

Figure S2C compares the number of fragmenting events for the particles to fragment from their surface size distribution into particles with $R \leq 5 \times 10^{-7}\,\mathrm{m}$ that were found at the sampling location. From the distribution we can see that the more size classes are considered in the fragmentation kernel, the fewer fragmentation events there are to reach the size distribution at the sampling location. We see that for most of the particles in the $k_{max} = 4$ simulation, it only took two fragmentation events, and for $k_{max} = 3$, the distribution becomes flatter, with 50% of the particles fragmenting three times and 40% of the particles fragmenting . For $k_{max} = 2$, most of the particles fragment three times, with a few cases fragmenting up to 7 times to reach the size distribution at the sampling location.

References

Al Harraq, A., & Bharti, B. (2022, January). Microplastics through the Lens of Colloid Science. *ACS Environmental Au*, *2*(1), 3–10. Retrieved 2022-11-28, from `https://doi.org/10.1021/acsenvironau.1c00016` (Publisher: American Chemical Society) doi: 10.1021/acsenvironau.1c00016

Russel, W. B., Saville, D. A., & Schowalter, W. R. (1989). *Colloidal Dispersions.* Cambridge: Cambridge University Press. Retrieved 2023-09-19, from `https://www.cambridge.org/core/books/colloidal-dispersions/A880F349E6ECA53C2E65D0FDEDABB091` doi: 10.1017/CBO9780511608810

Sutherland, B. R., DiBenedetto, M., Kaminski, A., & van den Bremer, T. (2023, July). Fluid dynamics challenges in predicting plastic pollution transport in the ocean: A perspective. *Physical Review Fluids*, *8*(7), 070701. Retrieved 2023-09-27, from `https://link.aps.org/doi/10.1103/PhysRevFluids.8.070701` (Publisher: American Physical Society) doi: 10.1103/PhysRevFluids.8.070701

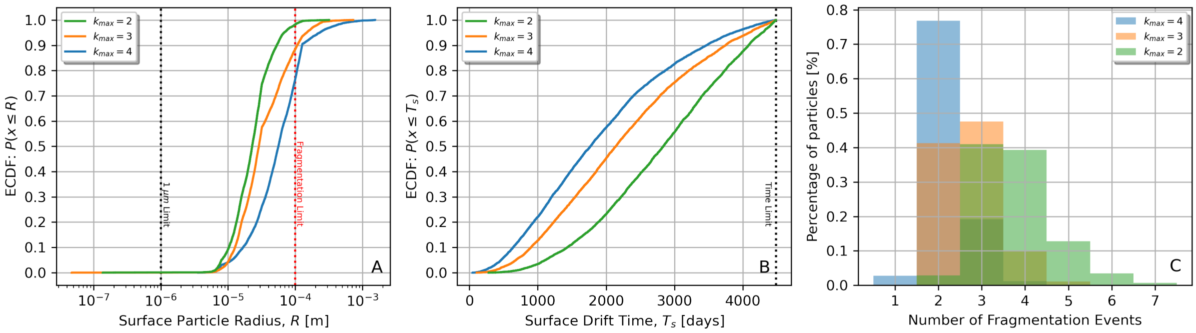

Figure S1. Comparison between simulations with maximum size class $k_{max} = 2$, $k_{max} = 3$, and $k_{max} = 4$, with a fixed fragmentation timescale $\lambda_f = 1000$ days. A) Empirical cumulative distribution function (ECDF) for the three simulations with different k_{max}. B) The ECDF for the time it takes the particles to go from the surface to the sampling location at $-5{,}000$ m deep, and therefore fragment from larger particles to particles with $R \leq 5 \times 10^{-7}$ m. C) The total number of fragmentation events needed for the particles to fragment from the surface size distribution into particles with $R \leq 5 \times 10^{-7}$ m, for the simulation with different k_{max}.

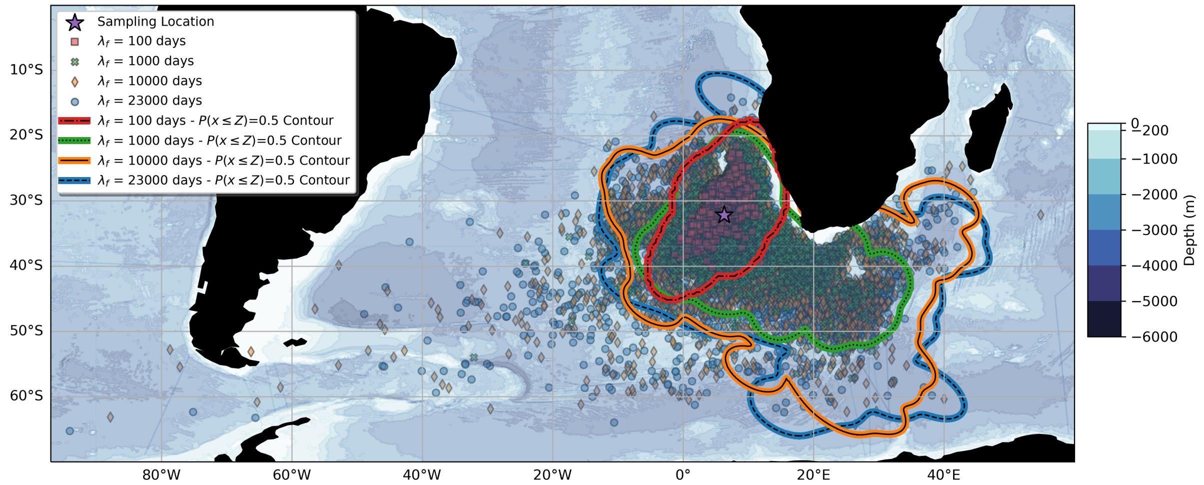

Figure S2. Map showing the location of where particles fragment into nanoplastics with radius $R < 1\,\mu m$. The star shows the sampling location for the nanoplastics. Each marker and color show the locations for simulations with different fragmentation timescale λ_f. The colored solid curves show the contours surrounding the location of particles where $P(x \leq Z) = 0.5$, show in Figure 6. The contours show how all nanoplastics originating in the depths $\leq -4{,}000$ m originated on the east side of the Mid Atlantic Ridge.

Table S1. The magnitude of the characteristic forces for microplastics in water. The table compares particles with radius $R = [0.01, 0.1, 1, 10, 100]$ µm. The assumed density of the particle is $\rho = 1{,}380\,\mathrm{kg/m^3}$, the PET density. The characteristic velocity for the respective particle radius is $U \approx [10^{-10}, 10^{-8}, 10^{-6}, 10^{-4}, 10^{-3}]\,\mathrm{m\,s^{-1}}$. The assumed values for the constants were $T \approx 273\,\mathrm{K}$, $\mu \approx 1 \times 10^{-3}\,\mathrm{kg\,m^{-1}\,s}$, $\Delta\rho \approx 380\,\mathrm{kg/m^3}$, and $g \approx 10\,\mathrm{m/s^2}$.

	$R =$	0.01 µm	0.1 µm	1 µm	10 µm	100 µm
$\frac{\text{Brownian force}}{\text{Viscous force}}$	$\frac{k_b T}{\mu R^2 U} \approx$	10^{8}	10^{4}	1	10^{-3}	10^{-6}
$\frac{\text{Buoyant force}}{\text{Viscous force}}$	$\frac{g \Delta\rho R^3}{\mu R U} \approx$	1	1	1	1	10
$\frac{\text{Inertial force}}{\text{Viscous force}}$	$\frac{\rho U^2 R^2}{\mu R U} \approx$	10^{-12}	10^{-9}	10^{-6}	10^{-3}	10^{-1}